Detailed characterisation of TiO_2 nano-aggregate morphology using TEM image analysis

Manoel Y. Manuputty[a,d], Casper S. Lindberg[a,d], Maria L. Botero[c,d], Jethro Akroyd[a,d], Markus Kraft[a,b,d,*]

[a]*Department of Chemical Engineering and Biotechnology, University of Cambridge, West Site, Philippa Fawcett Drive, Cambridge, CB3 0AS, United Kingdom*
[b]*School of Chemical and Biomedical Engineering Nanyang, Technological University, 62 Nanyang Drive, 637459, Singapore*
[c]*Department of Mechanical Engineering, National University of Singapore, 9 Engineering Drive 1, 117575, Singapore*
[d]*Cambridge Centre for Advanced Research and Education in Singapore (CARES), CREATE Tower, 1 Create Way, 138602, Singapore*

Abstract

A detailed morphological characterisation is performed on flame synthesised TiO_2 nano-aggregates (number of primaries, $N < 10$) using transmission electron microscopy (TEM) image analysis and mobility measurements. The size-dependent collection efficiency of the TEM sampling method is accounted for with a simple correction for particle deposition through impaction and diffusion. The TEM-derived sizes show excellent agreement with electrical mobility measurements. Primary particle size, aggregate size, and degree of aggregation distributions were obtained for two different flames and varying precursor loading. The analysis reveals some particle aggregation which is likely to occur only very late in the growth stage, leading to the similarity between the primary particle and spherical particle size distributions. The degree of aggregation is defined as the ratio of gyration to spherical equivalent sizes from the projected area analysis, allowing identification of particles with spherical and non-spherical morphologies. The size distributions are found to be strongly affected by precursor loading but not by flame mixture or maximum temperature. In all cases, approximately 60–70% particles are spherical while the rest form small aggregates. The detailed morphological information reported provides the much-needed experimental data for studying the early stage particle formation of TiO_2 from titanium tetraisopropoxide (TTIP) in a well-defined burner configuration.

Keywords: TiO_2, premixed flame, TEM, image analysis, nano-aggregates

*Corresponding author
Email address: mk306@cam.ac.uk (Markus Kraft)

1. Introduction

Combustion synthesis has been increasingly used to prepare functional metal oxide nanoparticles such as titanium dioxide (TiO_2) [20, 39]. In order to design and exploit this process, understanding of the complex chemical and physical processes involved in the conversion of gaseous precursor molecules to solid particles is required. Such understanding is the motivation behind experimental studies employing well-defined burners to synthesise and characterise TiO_2 nanoparticles [43, 29, 44, 16, 27]. These are complemented by the development of comprehensive computational models of such systems guided by experimental observations [48, 17].

Premixed stagnation flames have been used to prepare TiO_2 nanoparticles from titanium tetraisopropoxide (TTIP) with particle sizes of 4–15 nm [43, 29, 16, 27]. The small particle size and narrow distribution are a result of a very short particle residence time, ideal for studying the early stages of particle formation. Computationally, the pseudo one-dimensional flow in a stagnation flame reactor enables the coupling between the particle model with the detailed gas-phase chemistry and flow dynamics at relative ease [50, 26].

Techniques to investigate the nanoparticle formation in such a flame include electrical mobility sizer [52, 43], mass spectrometry [16], laser diagnostics [35], electron microscopy [29, 51], and X-ray diffraction [27, 51, 29]. Among these, electron microscopy imaging (i.e. TEM) is suitable to investigate the particle morphology [33, 46] as it reveals the actual structure of particles, albeit as 2D projection. For example, TEM image analysis has been widely used in the combustion community to measure morphological properties of soot, such as aggregate size and fractal dimension [10, 2, 6, 15]. The main challenges with TEM measurements are the sensitivity to the sampling technique [33] and the difficulty in achieving statistically significant sample size.

Mobility measurements have also been routinely used to characterise particle morphology as it enables easy and fast data acquisition [52, 9, 47]. However, the interpretation of mobility sizes is not straightforward [40, 21]. Previous comparative studies, both for soot and TiO_2, show some discrepancy between particle sizes measured with TEM and mobility sizer [43, 10]. Tolmachoff et al. [43], using a premixed stagnation flame setup, showed that TiO_2 particle sizes measured with a mobility sizer overestimate those derived from TEM measurements. The authors attributed this discrepancy to the difference in sampling conditions based on the assumption that particles are spherical. Nevertheless, it is likely that some aggregation occured in the gas phase, as evidenced from the TEM images, resulting in larger mobility sizes. Resolving such morphological information is essential in order to properly interpret the experimental data and evaluate computational models [26, 23].

Computational representation of particles often rely on certain simplifications to make the problem solvable [31]. The simplest representation is the spherical model where a particle is described only by its mass. This allows the number of population balance equations to be reduced and solved with moment-based methods [26, 11]. This description can be extended in different ways to

account for non-spherical morphology [44, 45, 49]. However, these often require making assumptions which are not always justified, such as particle monodispersity or power-law relationships for fractal-like aggregates, leading to additional uncertainties in the evaluation of the model parameters.

Alternatively, particles can be represented as an aggregate consisting of connected primary particles which can be solved stochastically [31, 30, 38, 4]. This detailed description resembles the actual structure of particles in experiments and thus the morphological properties can be derived without making unjustified assumptions. Recently, Lindberg et al. [24] proposed a new detailed particle model where the coordinates of individual primary particles are tracked and thus the full particle morphology can be resolved. This method has been demonstrated for modelling the particle population dynamics for premixed stagnation flame experiments [50, 14, 23]. However, the level of details that the model is capable of resolving requires comparison against similarly detailed morphological measurements which are currently lacking in the literature.

The purpose of this paper is to demonstrate a careful application of TEM image analysis and mobility measurements to characterise and interpret the morphology of small flame-synthesised TiO_2 nano-aggregates with small number of primaries ($N < 10$). The analysis quantifies the degree of aggregation in the nanoparticle prepared which explains the discrepancy between TEM derived and mobility sizes reported previously [43]. The quantification of aggregation proposed in this paper provides the much-needed morphological data for computational model evaluation. In this work, varying operating conditions, including temperature and precursor loading, are chosen to evaluate their effects on the synthesised particle morphology, such as primary particle size and the degree of aggregation.

The rest of this paper is structured as follows. Section 2 describes the experimental setup and the sampling procedures. Section 3 outlines the TEM image analysis algorithms used. Section 4.1 evaluates the sampling dilution ratio and its effect on the measured particle size and number density. Section 4.2 discusses the validation of the TEM sampling methodology by comparison with the electrical mobility measurements and Section 4.3 presents the morphological descriptions of the particles. Finally, the conclusions of this work are given.

2. Experimental methods

Figure 1 shows a schematic of the premixed laminar stagnation flame used in this study. Briefly, an aerodynamic nozzle (1.4 cm exit diameter) generated a laminar jet of premixed mixture that impinged on a water-cooled stagnation plate. Upon ignition, a thin flame was formed and stabilised by stretch above the stagnation plate. The setup used here is similar to that used in previous studies of titania and soot formation [43, 29, 9].

Two different flames were employed in this study with equivalence ratios of $\phi = 0.35$ (3.5% C_2H_4–30% O_2–66.5% Ar) and $\phi = 1.67$ (10.3% C_2H_4–18.5% O_2–71.2% Ar), corresponding to fuel-lean and fuel-rich conditions, respectively. The two different flames were used to investigate the effect of flame temperature with

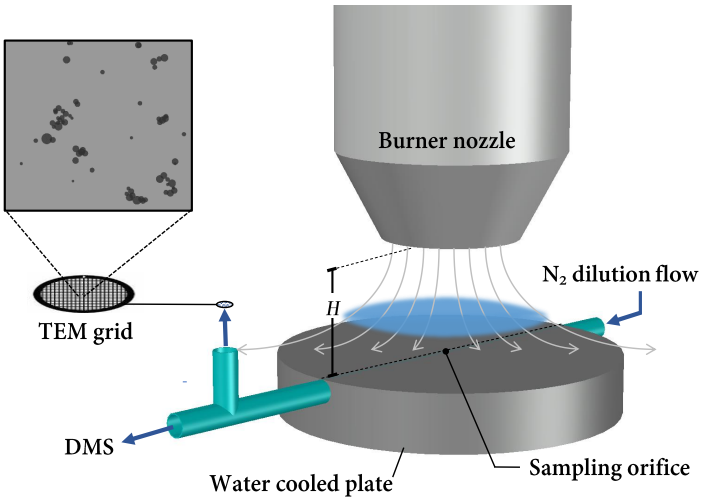

Figure 1: A schematic of the premixed laminar stagnation flame synthesis and particle sampling method used in this study. The burner-stagnation surface separation distance, H, is 1 cm.

the rich flame being approximately 450 K hotter than the lean flame based on the calculated adiabatic flame temperature (T_{ad} = 2073 K and 2542 K [27]). The total gas flowrate was 28 slpm with a N_2 sheath flowrate of 20 slpm. The burner-surface separation, H, was 1 cm. The surface temperature, measured with a K-type thermocouple, was stabilised at 503±20 K (ϕ = 0.35) and 580±20 K (ϕ = 1.67). The flame standing distance was approximately 3.2±0.2 mm (ϕ = 0.35) and 4.0±0.2 mm (ϕ = 1.67). For each flame, titanium tetraisopropoxide (TTIP, Sigma Aldrich, 97%) was injected into the gas line with a syringe pump (Cole-Parmer) at loading rates of 4, 12, and 30 ml/h (corresponding to 194, 582, and 1455 ppm of TTIP). The gas line was heated to 150°C to prevent precursor condensation. Previous studies have shown that the particles synthesised in the lean flame are mainly anatase while particles prepared in the rich flame are mainly mixtures of rutile and the metastable phase TiO_2-II [27].

Post-flame gas was sampled through a 0.2 mm orifice on a horizontal sampling probe inside the stagnation plate as shown in Fig. 1. The static pressure drop across the orifice was maintained at 4 ± 0.5 mbar under atmospheric pressure. The pressure drop is calculated as the average between the pressure drops upstream and downstream from the orifice measured using static pressure taps. A nitrogen flow of 36 l/min (STP) was used to quench the sampled gas to minimise further reactions after sampling and particle losses due to coagulation and wall deposition. Dilution tests were performed by varying the dilution (N_2) flow rate to assess the sensitivity of the measured particle size and number density to the dilution ratio, discussed further in Sec. 4.1. Downstream from the sampling orifice, a needle valve and vacuum pump system was configured to allow 8 l/min of the diluted flow to pass to a DMS500 (Cambustion Ltd.) for

electrical mobility size measurements. Simultaneously, the remaining diluted gas was passed through a TEM grid (HC400-Cu, Electron Microscopy Sciences) mounted perpendicular to the flow within the sample line where particles were deposited and subsequently imaged for analysis. The holey carbon grids were chosen to allow sufficient particle collection for analysis. The sampling time for each measurement was 10–15 s. TEM micrographs were obtained with a JEOL JEM-2100F operating at 200 keV.

3. Image analysis

The image analysis procedures for primary particle size distribution and aggregate size distributions were performed on images from the same TEM samples but taken at different magnifications and locations on the grid. The carbon film on the TEM grid contains holes with varying sizes and densities. For primary particle analysis, the images are taken at areas with high density of holes that has the "lacy" appearance. This results in high particle concentration and better contrast. For aggregate analysis, the images are taken at areas with low density of holes such that it is possible to have a complete film coverage, i.e. no holes, on the TEM images. This is to ensure a low particle concentration to minimise overlap and to allow image processing algorithm as described below.

For primary particle size analysis, approximately 20–30 images with 150,000× magnification were used (0.13 nm/pixel resolution) with minimum particle count of approximately 1100 (see Table 5). For aggregate size analysis, magnifications of 80,000× (0.24 nm/pixel), 60,000× (0.32 nm/pixel), and 40,000× (0.47 nm/pixel) were used for 4, 12, and 30 ml/h TTIP loading cases, respectively. The different magnifications were chosen to maintain a similar pixel count per particle across the TTIP loadings tested. Approximately 100 images per sample were used with minimum particle count of approximately 1500 (see Table 6).

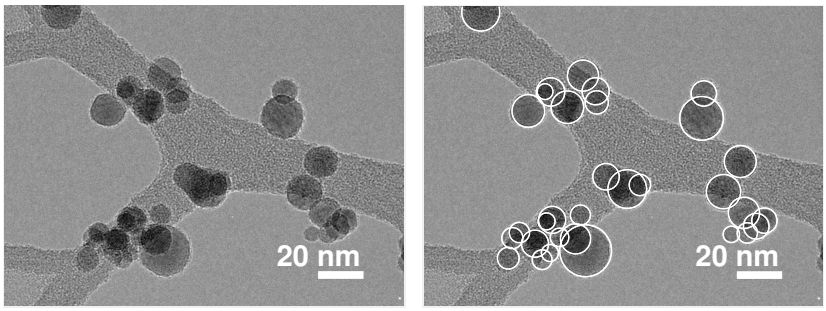

(a) A TEM image with 150,000× magnification.

(b) An annotated image showing spherical primary particles.

Figure 2: TEM images showing primary particle size measurement procedure employed (ϕ = 1.67, 30 ml/h TTIP loading rate).

Primary particle size analysis. For primary particle size analysis, the measurement of primary particle diameter, d_p, was performed using a MATLAB user interface by specifying the center of the sphere and a point on the circumference manually. The uncertainty of the measured d_p from manual measurement is estimated to be ± 2 pixel or ± 0.25 nm. Figure 2 shows an example of TEM images with spherical primary particles annotated. Due to the limited resolution of the TEM imaging, only particles larger than 3 nm were clearly distinguishable and measured. The average diameter ($\overline{d}_p$), Sauter mean diameter ($\overline{d}_{32}$), standard deviation (SD), and geometric standard deviation (GSD) were calculated for each case as follows,

$$\overline{d}_p = \frac{1}{N}\sum_{i=1}^{N} d_{p,i} \tag{1}$$

$$\overline{d}_{32} = \frac{\sum_{i=1}^{N} d_{p,i}^3}{\sum_{i=1}^{N} d_{p,i}^2} \tag{2}$$

$$\mathrm{SD} = \sqrt{\frac{1}{N-1}\sum_{i=1}^{N} |d_{p,i} - \overline{d_p}|^2} \tag{3}$$

$$\mathrm{GSD} = \exp\sqrt{\frac{1}{N}\sum_{i=1}^{N}\left(\ln\frac{d_{p,i}}{\mu_g}\right)^2}, \tag{4}$$

where $d_{p,i}$ is the spherical equivalent diameter of an individual primary particle, N is the total number of primary particles measured, and μ_g is the geometric mean of the measured data set $\{d_{p,1}, d_{p,2}, ..., d_{p,N}\}$.

Aggregate size analysis. For aggregate projected area analysis, the following semi-automated procedures were employed (see Fig. 3 for illustration) using built-in functions in MATLAB Image Processing Toolbox [28],

1. **Filters**: Perform a contrast-limited adaptive histogram equalization (*adapthisteq* function) on 3×3 pixel tiles followed by a 2-D median filtering (*medfilt2* function) on 4×4 pixel tiles to enhance image contrast and reduce "salt and pepper" noise.
2. **Binarization**: Create a binary image with adaptive image threshold calculated using local first-order image statistics around each pixel (*imbinarize* function). A dark foreground polarity and a sensitivity parameter of 0.05 were specified.
3. **Rolling ball 1-4**: Restructure connected black pixels with four successive rolling ball transformations (*strel* function, [12]) with increasing disk size of 0.6 (rolling ball 1), 0.8 (rolling ball 2), 1.2 (rolling ball 3), and 1.6 nm (rolling ball 4).
4. **Edges removal**: Remove pixel blobs that touch the image edges to exclude aggregates that are not completely within the image frame.

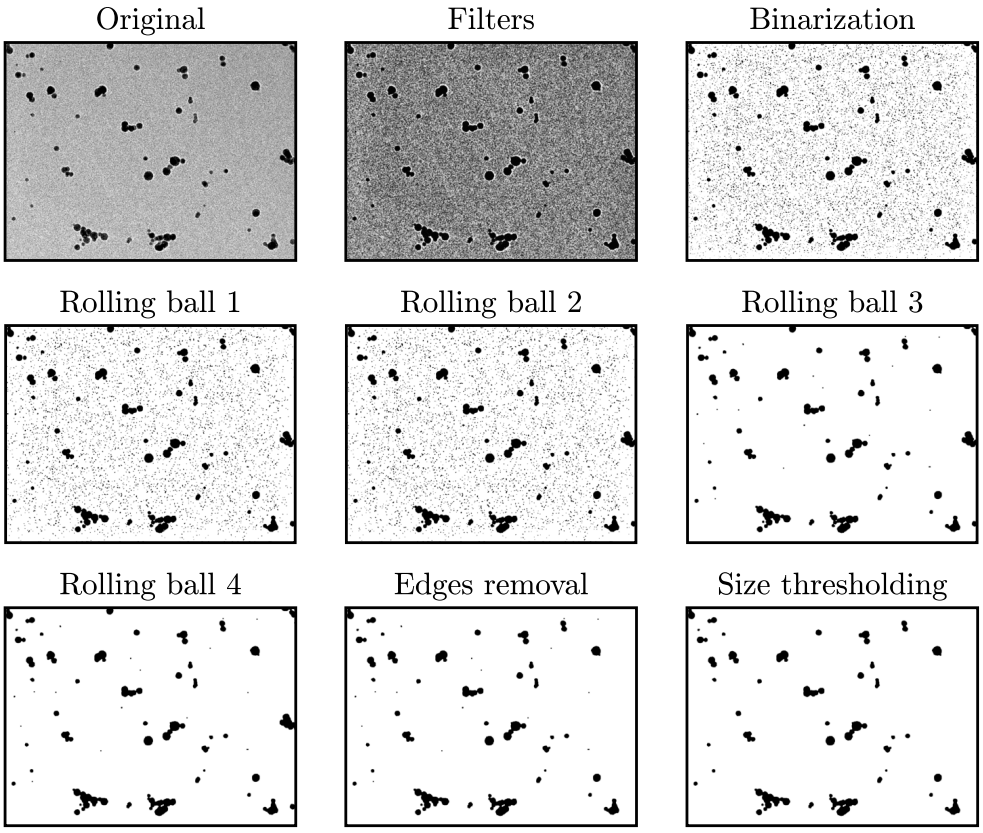

Figure 3: Snapshots of an analysed TEM image (ϕ = 1.67, 30 ml/h TTIP loading rate) at different stages of the projected area analysis procedure.

5. **Size thresholding**: Remove structures with spherical equivalent diameter smaller than a specified threshold (2, 3, and 4 nm for 4, 12, and 30 ml/h loading rates, respectively).
6. Lastly, in the rare instance that the algorithm results in structures that are not particles (e.g., from clustered noise), these false particles are removed manually.

From the aggregate analysis, a data set $\{\mathbf{P}_1, \mathbf{P}_2, ..., \mathbf{P}_N\}$ was obtained where $\mathbf{P}_i$ contains a list of coordinates of the constituent pixels of aggregate i: $\{(x_{i,1}, y_{i,1}), (x_{i,2}, y_{i,2}), ..., (x_{i,L}, y_{i,L})\}$. The projected spherical equivalent diameter ($d_{\mathrm{sph},i}$) and the projected diameter of gyration ($d_{g,i}$) of aggregate i

were calculated as follows,

$$d_{\mathrm{sph},i} = 2s\sqrt{\frac{L}{\pi}} \tag{5}$$

$$d_{g,i} = s\sqrt{\frac{1}{L}\sum_{j=1}^{L}\left(|x_{i,j} - \overline{x_i}|^2 + |y_{i,j} - \overline{y_i}|^2\right)} \tag{6}$$

$$(\overline{x_i}, \overline{y_i}) = \frac{1}{L}\sum_{j=1}^{L}(x_{i,j}, y_{i,j}), \tag{7}$$

where s is the image scale factor (nm per pixel) and L is the total number of pixels for aggregate i. Additionally, a parameter α_i was defined as the ratio of $d_{g,i}$ to $d_{\mathrm{sph},i}$, which is indicative of the degree of aggregation of an analysed particle. A projected sphere, i.e. circle, has a characteristic $\alpha = \sqrt{1/2} \approx 0.71$, while for a projected dimer with no overlap, $\alpha = \sqrt{3/4} \approx 0.87$. However, calculation of radius of gyration according to Eq. 6 tends to be an overestimate for a pixelated circle with less than 100 pixels and thus the value of α is expected to be slightly larger than 0.71 for a projected sphere (this is discussed further in Section 4.3). The average aggregate projected area, $\overline{d}_{\mathrm{sph}}$, and the average projected aggregate gyration diameter, $\overline{d}_g$, were calculated as follows,

$$\overline{d}_{\mathrm{sph}} = \frac{1}{N}\sum_{i=1}^{N} d_{\mathrm{sph},i} \tag{8}$$

$$\overline{d}_g = \frac{1}{N}\sum_{i=1}^{N} d_{g,i}, \tag{9}$$

where N is the total number of aggregates identified in the analysis.

The projected diameter gyration, d_g, calculated in Eq. 6 is not equivalent to the actual diameter of gyration, $d_g^{3\mathrm{D}}$, typically used in the literature. For fractal aggregates with fractal dimension, $D_f > 2$, the following relationship applies [8]

$$d_g^{3\mathrm{D}} = \left(\frac{2D_f}{Df + 2}\right)^{1/2} d_g. \tag{10}$$

This equation implies a correction factor of 1.095 for a compact sphere (number of primary particles, $N = 1$, $D_f = 3$). For $N = 2$, assuming no particle screening effect, both gyration sizes are exact and can be derived analytically ($d_g^{3\mathrm{D}} = \sqrt{8/5}d$, $d_g = \sqrt{3/2}d$, d = primary diameter) resulting in a correction factor of 1.033, equivalent to $D_f = 2.3$ according to Eq. 10. For mature aggregates with $D_f \leq 2$, typical for soot, Sorensen and Feke [41] calculated a conversion factor of 1.023. In this work, TEM images (as discussed later) show a significant proportion of particles with N ranging from 1 to 4. As shown above, the conversion factor shows dramatic change from $N = 1$ (sphere) to $N = 2$

(dimer) while for larger aggregates, this conversion factor is almost constant [40, 41]. Thus the conversion to the actual gyration diameter would introduce significant additional uncertainty in this work due to the large variance in the particle fractal dimension. In addition, for the purpose of defining the particle morphology, α calculated with the projected diameter of gyration is sufficient (see Section 4.3). For these reasons, the conversion of the gyration sizes is not performed here.

4. Results and discussion

4.1. Sampling dilution

Given the large number density of particles sampled from the flame, sample dilution is necessary to minimise particle losses due to coagulation and deposition on the wall and the orifice. Sample dilution also cools and quenches the sampled gas to prevent further reactions. A thorough study on the dilution behaviour of a similar sampling system has been performed by Zhao et al. [53] who used a dilution flow of 29.5 l/min. The purpose of this section is to evaluate the sensitivity of the particle size and number density to the dilution ratio for the measurement conditions used in this work.

Here the dilution ratio is varied by changing the dilution volumetric flow rate, L = 15–38 l/min (STP), within the sampling line while maintaining a small static pressure drop, $\Delta P_o = P_{\mathrm{atm}} - P_o$, approximately 4 ± 0.5 mbar across of the orifice. Each measurement is averaged over 5 seconds (with data acquisition rate of 10 Hz). This pressure drop is sufficiently small to avoid flame perturbation and large enough to prevent counterflow at the orifice due to pressure fluctuation during measurements. The total pressure drop, ΔP, is thus

$$\Delta P = \Delta P_o - \frac{\rho}{2A^2} L^2, \tag{11}$$

where the second term represents the dynamic pressure given as a function L, ρ, the mass density, and A, the flow cross section. For L = 36 l/min (flow rate used in this this work), the dynamic pressure is approximately 3.7 mbar. The sampled gas volumetric flow rate, L_s, is calculated using the relation for pressure loss due to laminar flow in a circular pipe,

$$L_s = \frac{f \pi d_o^4}{l \mu} \Delta P = k \Delta P, \tag{12}$$

where f is the friction factor, d_o is the orifice diameter, l, is the orifice length, μ is the gas viscosity. Assuming f, d_o, l, and μ are constant during the measurements, k was obtained from calibration using flow meters (≈ 7.6 ml·min^{-1}mbar^{-1}). The total dilution ratio, DR, is subsequently calculated similar to [53], i.e. DR $= 3.4L/L_s$. The calculated DRs for all dilution flow rates tested are shown in Fig. 4.

Figure 5(a) shows the measured particle number density measured by the DMS500 as a function of DR for the $\phi = 0.35$ flame with 12 ml/h TTIP loading.

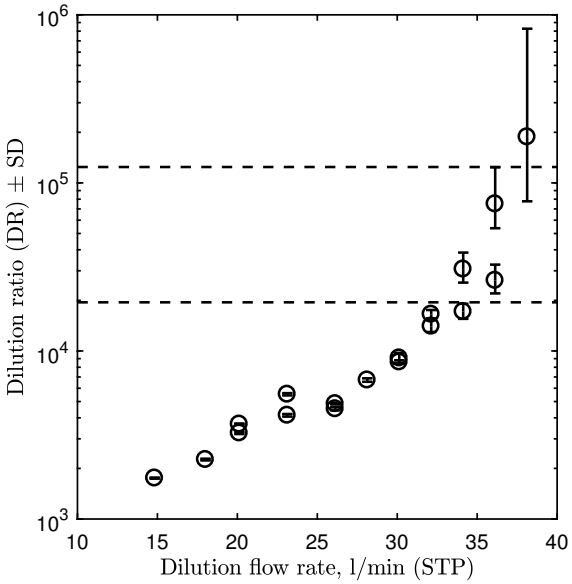

Figure 4: The calculated dilution ratio, DR, and standard deviation, SD, as a function of the dilution flow rate. The errorbar is calculated using the standard deviation of the pressure drop measurements. The dashed lines represent the range of DR for 36 l/min (STP) dilution flow rate given a fluctuation in the pressure drop in the range of 3.8–4.5 mbar.

It is clear that the number density increases with DR for low dilution range, i.e. DR $< 10^4$. For DR $> 10^4$, the number density converges to approximately 1.1×10^8 cm^{-3} within the measurement uncertainty (shaded region in Fig. 5(a)), suggesting that particle losses are sufficiently minimised. Figure 5(b) shows the change in particle size as a function of DR. Increasing DR results in smaller particle size as particle losses, both through coagulation and deposition, result in a shift of particle size distributions towards a larger size. The particle size similarly converges to approximately 12.3 ± 0.25 nm at high dilution (DR $> 2\times10^4$) as indicated by the shaded region.

Elsewhere this work, a dilution flow rate of 36 l/min and a static pressure drop fluctuation in the range of 3.8–4.5 mbar (due to the difficulty in controlling the pressure drop) were used. These conditions correspond to a DR of approximately 0.2–1.2×10^5. This range is indicated with the dashed lines in Figs. 4 and 5. Within this range, Fig. 5 suggests that the particle number density and size are relatively insensitive to the dilution ratio.

4.2. Validation of TEM sampling methodology

The TEM sampling methodology employed in this work is distinct to thermophoretic sampling commonly used for in-situ particle sampling [2, 6, 3]. Instead of thermophoresis, the particle deposition here relies on two main physical mechanisms, namely inertial impaction and Brownian diffusion as the sample flow through the holey TEM grid suspended perpendicular to the flow direction.

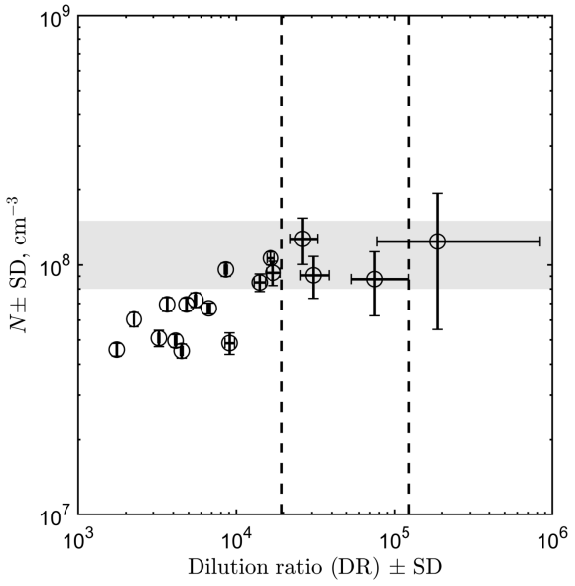

(a)

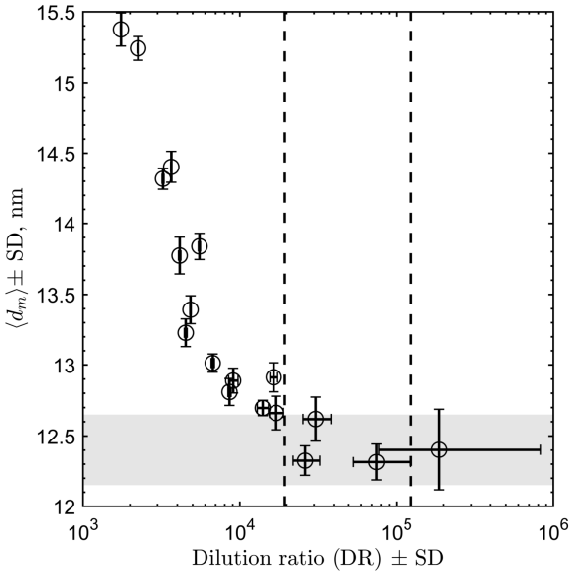

(b)

Figure 5: (a) Particle number density, N, and (b) median particle size, $\langle d_m \rangle$, and the respective standard deviations, SD, as a function of dilution ratio, DR, for $\phi = 0.35$ flame and 12 ml/h TTIP loading. The dashed lines represent the range of DR for 36 l/min (STP) dilution flow rate given a fluctuation in the pressure drop in the range of 3.8–4.5 mbar. The shaded regions indicate the converged values of N and D_m and the corresponding experimental uncertainties at high DR.

It is assumed that interception can be ignored here given the size of the holes on TEM grid is typically much larger than the particles [36].

Due to the size dependency of inertial impaction and Brownian diffusion, it is necessary to perform a correction to the particle size distributions obtained using this methodology. However, as demonstrated below, the narrow size distribution produced with the stagnation flame configuration combined with the high sampling flow velocity results in a minimal correction. In this section, the overall collection efficiency of the holey TEM is estimated using similar approach used by Ogura et al. [32]. Subsequently, the corrected particle size is validated by comparison with the electrical mobility diameter measured with the DMS.

4.2.1. Correction for TEM collection efficiency

Taking into account Brownian diffusion and inertial impaction, assuming both mechanisms act independently, the overall collection efficiency, E, can be expressed as

$$E = 1 - (1 - E_{\mathrm{D}})(1 - E_{\mathrm{I}}), \tag{13}$$

where E_{D} is the collection efficiency due to Brownian diffusion, and E_{I} is the collection efficiency due to inertial impaction.

Brownian diffusion. The collection efficiency due to particle diffusion to the front surface of a filter can be calculated using an expression proposed by Manton [25],

$$E_{\mathrm{D}} = 1 - \exp\left(\frac{-\alpha_1 \mathrm{Pe}^{-2/3}}{1 + (\alpha_1/\alpha_2)\mathrm{Pe}^{-7/15}}\right) \tag{14}$$

$$\alpha_1 = 4.57 - 6.46 P_{\mathrm{grid}} + 4.58 P_{\mathrm{grid}}^2 \tag{15}$$

$$\alpha_2 = 4.5, \tag{16}$$

where Pe is the Peclet's number given by $\mathrm{Pe} = D_0 U_0 / D$, D_0 is the grid hole diameter, U_0 is the frontal velocity, P_{grid} is the grid porosity, α_1 and α_2 were determied from a least-squares fitting for $0.05 < P_{\mathrm{grid}} < 0.64$. D is the particle diffusion coefficient,

$$D = \frac{k_{\mathrm{B}} T C_c}{6\pi\mu R}, \tag{17}$$

where k_B is the Boltzmann constant, T is the temperature, μ is the gas dynamic viscosity, R is the particle radius. C_c is the Cunningham slip correction factor given by

$$C_c = 1 + \mathrm{Kn}(1.257 + 0.4\exp(-1.1/\mathrm{Kn})), \tag{18}$$

where Kn is the Knudsen number defined as λ/R and λ is the mean free path of the gas molecules.

Inertial impaction. The collection efficiency due to particle impaction is calculated using a formulation proposed by Pich [34] as follows,

$$E_I = \frac{2\epsilon_I}{1+\xi} - \left(\frac{\epsilon_I}{1+\xi}\right)^2 \tag{19}$$

$$\epsilon_I = 2\mathrm{Stk}\sqrt{\xi} + 2\mathrm{Stk}^2\xi \exp\left(-\frac{1}{Stk\sqrt{\xi}}\right) - 2\mathrm{Stk}^2\xi \tag{20}$$

$$\xi = \frac{\sqrt{P_{\mathrm{grid}}}}{1-\sqrt{P_{\mathrm{grid}}}}, \tag{21}$$

where Stk is the Stokes number given by

$$\mathrm{Stk} = \frac{4\rho_s R^2 U_0 C_c}{9\mu D_0}, \tag{22}$$

and ρ_s is the particle density.

In this analysis, the particle size is assumed to be equal to the spherical equivalent size from projected area analysis, i.e. $2R = d_{\mathrm{sph}}$. This assumption is a valid approximation given that the particles observed on the TEM are mostly single primaries with some small aggregates (discussed further in Section 4.3). The parameters used in the calculation of TEM grid collection efficiency (Eq. 13) are given in Table 1. The face velocity is approximately 14 m/s, estimated from the total flow rate flowing through the filter (27 lpm) and the tube cross-section area (32 mm^2). However, the actual face velocity is likely to be lower due to flow divergence on the TEM surface. As an estimate, two different face velocities are tested here, 14 and 7 m/s. The hole diameter and grid porosity are taken from Ref. [36] for a typical holey carbon grid. The density of anatase is used for particles prepared in $\phi = 0.35$ flames while density of rutile is used for $\phi = 1.67$ [27, 29].

Table 1: Parameters used for size-dependent collection efficiency calculation.

Parameters	Short description	Value	Notes
λ	Mean free path	70.9 nm	N_2 at 313.15 K, 1 atm
μ	Gas dynamic viscosity	1.85×10^{-5} kg/m/s	N_2 at 313.15 K
ρ_s	Anatase density	3780 kg/m^3	For $\phi = 0.35$
	Rutile density	4250 kg/m^3	For $\phi = 1.67$
T	Gas temperature	313.15 K	Experimental condition
U_0	Face velocity	7 and 14 m/s	Experimental condition
D_0	Hole diameter	1.67 μm	[36]
P_{grid}	Grid porosity	0.4	[36]

The calculated collection efficiency is shown in Fig. 6(a). This correction is applied to the aggregate size distributions from the TEM image analysis. In order to demonstrate the effect of this correction across the conditions studied

in this work, the median spherical-equivalent particle sizes, $\langle d_{\mathrm{sph}} \rangle$, for $\phi = 0.35$ flame, before and after correction, are plotted in Fig. 6(b). It is noted that the correction is relatively small, especially for small TTIP loadings which is due to narrow particle distributions. In addition, the correction seems to be almost insensitive to the choice of face velocity. Subsequently, similar correction with $U = 7$ m/s is applied to all TEM aggregate particle size distributions presented in this work. This correction, however, is not applied for primary particle size distributions as the collection efficiency is a function of the aggregate size.

4.2.2. Comparison with electrical mobility measurements

The DMS500 used in this study was calibrated at the factory against a differential mobility analyzer (DMA). Here, calibration for spherical particles with a monomodal distribution was used. The Stokes-Cunningham formula for electrical mobility, Z, used with the DMA, is given by

$$Z/q = \frac{C_c}{6\pi\mu R}, \tag{23}$$

where q is the charge in the particle. The empirical Stokes-Cunningham formula is typically consistent with Eipstein's formula assuming a diffuse scattering model. However, it has been shown that in the limit of Kn >> 1, the mobility particle size based on the Stokes-Cunningham formula tends to be over-predicted by 10–20% compared to particle size from electron microscopy due to increasing influence of long-range potential forces on particle scattering [37, 18, 22].

Li and Wang [21] suggests a generalised expression that accounts for gas-particle interactions in Kn >> 1 limit,

$$Z/q = \frac{3}{8}\frac{1}{\sqrt{2\pi m_r k_{\mathrm{B}} T} N_g R^2 \Omega_{\mathrm{avg}}^{(1,1)^*}} \tag{24}$$

$$\Omega_{\mathrm{avg}}^{(1,1)^*} = \varphi \Omega_{\mathrm{d}}^{(1,1)^*} + (1-\varphi)\Omega_{\mathrm{s}}^{(1,1)^*}, \tag{25}$$

where m_r is the reduced mass of the gas molecule, m_g, and particle, m_p, such that $m_r = m_g m_p/(m_g + m_p)$, N_g is the gas number density given by ρ_g/m_g, ρ_g is the gas density. φ is the empirical momentum-accommodation function given by

$$\varphi = \frac{1 + 0.9\mathrm{Kn}\{1 - 1/[1 + (R/\beta)^{15}]\}}{1 + \mathrm{Kn}}, \tag{26}$$

where $\beta = 2.5$ nm. $\Omega_{\mathrm{d}}^{(1,1)^*}$ and $\Omega_{\mathrm{s}}^{(1,1)^*}$ are reduced collision integrals, parameterised as functions of σ', a non-dimensionalised collision diameter, and T^*, a modified reduced temperature. The parameters σ' and T^* are related to the Lennard-Jones 12-6 parameters, i.e. wall depth, ϵ, and collision diameter, σ, for the interaction between a fluid molecule and a constituent atom or molecule of

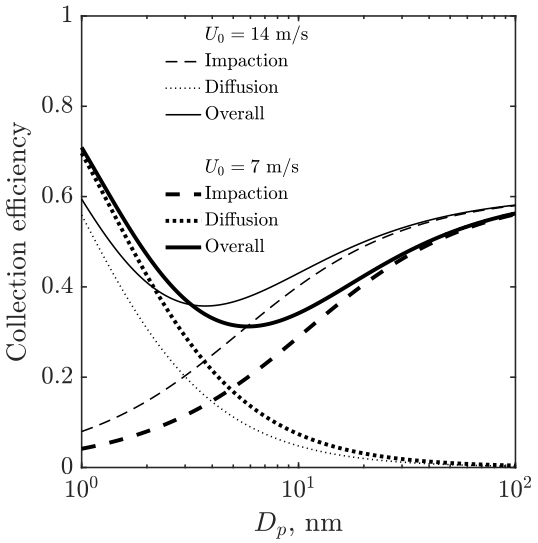

(a)

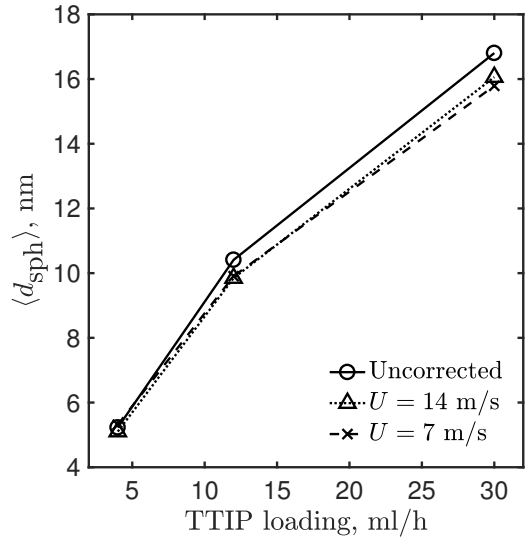

(b)

Figure 6: (a) The collection efficiencies calculated based on Eqs. 13, 14, and 19 with face velocities, U, of 7 and 14 m/s (thick and thin lines, respectively), using anatase density. (b) The median spherical-equivalent particle sizes, $\langle d_{\mathrm{sph}} \rangle$, before and after collection efficiency correction for $\phi = 0.35$ flames. The lines are added as a visual aid.

the particle, as follows,

$$\sigma' = \frac{\sigma}{R} \tag{27}$$

$$T^* = \frac{3Vk_{\mathrm{B}}T}{2\pi\epsilon\sigma^3}, \tag{28}$$

where V is the effective volume of the particle per molecule given by $\bar{M}/\rho_{\mathrm{s}}$, $\bar{M}$ is the mean atomic mass of particle material, and ρ_{s} is the mass density of the particle. The interaction potential parameters, σ and ϵ, can be estimated from the combination rules $\sigma = (\sigma_g + \sigma_s)/2$ and $\epsilon = \sqrt{\epsilon_g \epsilon_s}$, where subscripts g and s denote the gas molecule and particle molecule or atom.

The parameters σ_s and ϵ_s for TiO_2 are estimated using the melting point, T_m, and the mass density at melting point, ρ_{s,T_m}, of TiO_2, such that $\epsilon_s = 1.92kT_m$, and $\sigma_s = \sqrt[3]{1.8\bar{M}/\rho_{s,T_m}}$ [37]. Here the melting point of TiO_2 is taken as 2250 K and the density at melting point is 3210 kg/m^3 [1]. The parameters used in this section are summarised in Table 2. Similar to the TEM collection efficiency correction, the density of anatase is used for particles prepared in $\phi = 0.35$ flames while density of rutile is used for $\phi = 1.67$ [27, 29]. The working pressure and temperature of the DMS500 used in this analysis are 250 mbar and 50°C.

Table 2: Parameters used for mobility size correction.

Parameters	Short description	Value	Notes
μ	Gas viscosity	1.89×10^{-5} kg/m/s	N_2 at 323.15 K
λ	Mean free path	294 nm	N_2 at 323.15 K, 250 mbar
ϵ_g	L-J 12-6 parameter	98.4 K	N_2 [22]
σ_g	L-J 12-6 parameter	3.652 Å	N_2 [22]
ϵ_s	L-J 12-6 parameter	4320 K	TiO_2
σ_s	L-J 12-6 parameter	4.193 Å	TiO_2
m_g	Gas molecule mass	28.0 g/mol	N_2
ρ_g	Gas density	0.261 kg/m^3	N_2 at 323.15 K, 250 mbar
$\bar{M}$	Particle mass	79.9 g/mol	TiO_2
ρ_{s}	Anatase density	3780 kg/m^3	For $\phi = 0.35$
	Rutile density	4250 kg/m^3	For $\phi = 1.67$
T	Temperature	323.15 K	Experimental condition

The correction to the mobility diameter is performed by firstly calculating the electrical mobility, Z/q, based on Eqs. 18 and 23 for each size class of the DMS500 [5]. The calculated Z/q is used to solve for the corrected size classes according to Eq. 24. The corrected size distribution is then fitted with a log-normal distribution to obtain the median particle size, $\langle d_m \rangle$, and the geometric standard deviation, σ_g.

The uncertainty of the corrected mobility sizes is evaluated here by considering two parameters used in the correction which have the highest uncertainties,

particle density ρ_s, and β from Eq. 26. As discussed before, the particle density was chosen based on the major phase identified with powder diffraction [27] for the given equivalence ratio. However, this does not take into account mixtures of phases with different densities or possibility of a size-dependent density which can result in higher or lower effective density. Here a maximum uncertainty for ρ_s is taken as 20%, approximately representing the difference between the densest and the least dense phases observed [27]. The parameter β represents the crossover size between specular to diffuse scatterings. Li and Wang [22] determined this empirically to be 2.5 nm using the available experimental data for Ag and Cu while other studies suggested smaller values, i.e. 1–2 nm [42]. Thus the uncertainty for β is estimated to be ± 1 nm. These values are used to calculate the sensitivity of the median particle sizes for all cases in Table 3. The results suggest that the median sizes are relatively insensitive to the density (approximately 1% change for all cases). Similar insensitiviy is observed for β except for the 4 ml/h loading cases with larger β (maximum change of 8%). This is expected as the particle sizes for the low loading cases are close to the crossover size. The uncertainties shown in Table 3 are comparable to the average error calculated by Li and Wang [22], i.e. 7%.

Table 3: Sensitivity of the median mobility size after correction to particle density ρ_s and momentum accomodation function parameter β. Reference values for ρ_s are given in Table 2 while the reference $\beta = 2.5$ nm.

ϕ	TTIP (ml/h)	Change in $\langle d_m \rangle$, %			
		$\rho_s = 0.8\rho_s$	$\rho_s = 1.2\rho_s$	$\beta = 1.5$ nm	$\beta = 3.5$ nm
0.35	4	1.6	-1.2	-1.4	7.9
0.35	12	1.1	-0.9	-0.0	0.8
0.35	30	0.9	-0.7	-0.0	0.2
1.67	4	1.4	-1.1	-0.4	4.1
1.67	12	1.1	-1.1	-0.1	0.7
1.67	30	0.9	-0.8	-0.0	0.2

Finally, the uncorrected and corrected mobility sizes are compared with the spherical equivalent sizes for all cases in this work, shown in Fig 7(a). Here the error bars represent the estimated error of 7% in addition to the measurement uncertainty of ± 0.25 nm (Fig. 5) for the mobility sizes and the uncertainty due to the resolution of the TEM images (± 0.24 nm, ± 0.32 nm, ± 0.47 nm for the 4, 12, and 30 ml/h TTIP loading cases, respectively) for the spherical equivalent sizes. The comparison is further summarised in Table 4. As the DMS500 resolution is limited, a lower cutoff point of 3.8 nm–equivalent to the smallest DMS500 size class of 4.9 nm after correction–is applied to the spherical equivalent size data from the TEM image analysis. The resulting distribution is then fitted with a truncated log-normal distribution to obtain the median particle size, $\langle d_{\mathrm{sph}} \rangle$, and the geometric standard deviation, σ_g. The TEM-derived sizes are taken as the reference particle sizes for error calculation as a significant proportion of the

particles are spherical (discussed further in the next section). As expected, the discrepancy for uncorrected mobility size is greatest for the smallest particles. The correction applied reduces the average difference from 19% to 4%, similar to the average difference reported by Li and Wang [22] for previous experimental data.

Table 4: Particle sizes from TEM projected area analysis and mobility measurements, before and after correction, with the DMS.

ϕ	TTIP (ml/h)	TEM		DMS			DMS, corrected		
		$\langle d_{\text{sph}} \rangle$ (nm)	σ_g	$\langle d_m \rangle$ (nm)	Err. (%)	σ_g	$\langle d_m \rangle$ (nm)	Err. (%)	σ_g
0.35	4	5.69	1.50	7.25	27.4	1.30	5.73	0.8	1.34
0.35	12	9.70	1.62	12.27	26.5	1.38	10.43	7.6	1.44
0.35	30	15.37	1.58	15.96	3.8	1.39	13.99	-9.0	1.45
1.67	4	7.11	1.52	8.81	23.9	1.34	7.10	-0.1	1.40
1.67	12	9.80	1.63	11.81	20.5	1.35	9.94	-1.4	1.40
1.67	30	13.85	1.61	15.12	9.1	1.38	13.12	-5.3	1.43
		Mean absolute error, %			18.5			4.0	

Figure 7(b) shows the corrected and uncorrected mobility size distributions as well as the spherical-equivalent size distribution obtained from the TEM image analysis for $\phi = 1.67$ and 4 ml/h TTIP loading where the mobility measurement overpredicts the particle size by approximately 24%. This is consistent with previous studies comparing mobility and microscopy sizes where average overprediction of 20% was reported [37, 18]. The applied correction results in a much better agreement between the mobility and spherical equivalent median sizes.

However, some discrepancies are observed for the distribution widths as indicated by the geometric standard deviations, σ_g, also tabulated in Table 4. The TEM-derived size distributions has an average σ_g of 1.58 compared to 1.36 and 1.41 for uncorrected and corrected mobility size distributions, respectively. The broadening of the mobility size distributions after correction is a result of the size-dependent correction (i.e. larger correction for smaller particles). As a comparison, Tolmachoff et al. [43] reported σ_g of 1.3-1.5 for similar TTIP loading range. Similar discrepancy between the TEM and DMS distribution widths has been observed in other comparative studies before [10, 18] although the reason is unclear. Here, two possible reasons are suggested which will be inverstigated in further studies. First, the TEM image analysis does not always capture the projected particle shape precisely due to multiple factors including image quality as discussed in Section 3. For example, the aggregates can be artificially combined when the projections are too close or fragmented when some parts of the particles are not on the focus plane. These measurement errors result in broadening of the actual distributions. Second, the mobility size distributions measured by the DMS500, especially the widths, are sensitive to the classifier

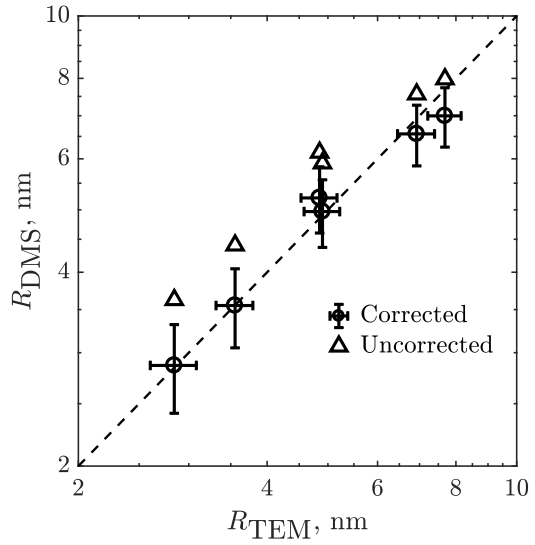

(a)

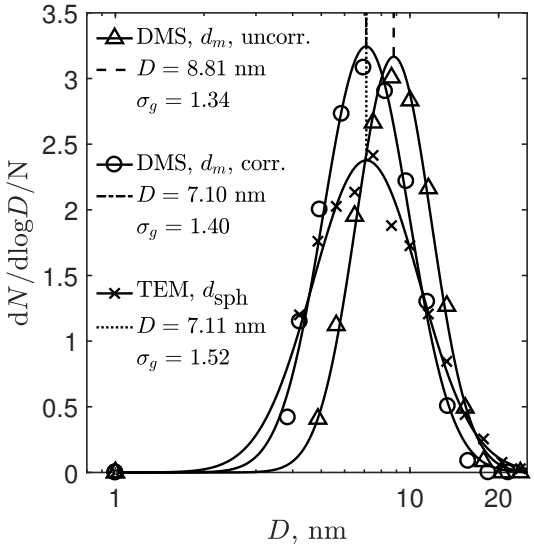

(b)

Figure 7: (a) Comparison between TEM-derived radii, R_{TEM}, and the mobility radii, R_{DMS}, corrected and uncorrected. The interpretation of the errorbars is discussed in the text. (b) Particle size distributions measured using DMS, d_m, corrected and uncorrected, and from TEM image analysis, d_{sph}, for ϕ = 1.67 and 4 ml/h TTIP condition. The vertical lines indicate the median values from log-normal fit to the distributions used in the correction. The geometric standard deviations, σ_g, are also indicated.

transfer function used by the DMS500 [5]. This is represented by the internal calibration matrices generated by the supplier (Cambustion Ltd.) with different aerosol standards. For example, the same measurements performed with calibration matrix generated with soot agglomerates tends to produce significantly broader distribution than those with calibration matrix generated with spherical aerosols although the median sizes are similar (unpublished data). The aggregate particle morphology could also affect the particle charge distribution from the unipolar diffusion charger [13, 19]. However, this is unlikely to be significant as the majority of particles are spherical or have low aspect ratio and therefore well described by the Fuchs' limiting-sphere theory as employed in the DMS500 charging model [5].

The close agreement between the corrected mobility particle size and TEM-derived particle size confirms that the sampling methodology used in this work can be used to characterise the morphology of small nano-aggregates as discussed in the next section.

4.3. Particle morphology

Table 5 summarises the measured primary particle sizes from the TEM images with high magnification (150,000×). It is important to point out that due to the resolution limit, poorer contrast, and higher chance of overlap, smaller particles are harder to measure manually (with only particles larger than approximately 3 nm can be confidently identified). This is likely to result in slight bias towards larger particles. As such, the Sauter mean diameter, $\bar{d}_{3/2}$, is reported here in addition to the averaged mean, $\bar{d}_p$, as it tends to represent data closer to the right end of the distribution. The primary particle distributions are relatively narrow as indicated by the geometric standard deviations, σ_g.

Table 5: Summary of primary particle analysis.

ϕ	TTIP (ml/h)	Primary particles			
		count	$\bar{d}_p \pm$ SD, nm	σ_g	$\bar{d}_{3/2}$, nm
0.35	4	1462	5.9 ± 1.3	1.25	6.5
0.35	12	1427	9.3 ± 2.4	1.29	10.6
0.35	30	1323	11.9 ± 3.7	1.37	14.3
1.67	4	1121	6.2 ± 1.3	1.23	6.8
1.67	12	1637	8.4 ± 2.2	1.30	9.5
1.67	30	1136	12.1 ± 3.3	1.33	13.9

Table 5 suggests that the primary sizes are strongly affected by the TTIP loading but are relatively insensitive to the flame temperature. This is surprising as the rich flame ($\phi = 1.67$) is approximately 450 K hotter than the lean flame ($\phi = 0.35$). This result is consistent with previous measurements which showed that the primary particle sizes from flames with a wide range of equivalence ratios with the same TTIP loading are similar [27]. The insensitivity of particle size to the maximum flame temperature was explained by the reduced particle residence time in hotter flames due to a higher convective velocity.

Figure 8 shows the TEM images used for the aggregate projected area analysis (see Section 3). The particle morphology can be described as a mixture of single spherical particles and small aggregates with small degree of sintering. High magnification experimental TEM images, not shown here, reveal highly crystalline primary particles. These observations are in agreement with previous studies [29, 43].

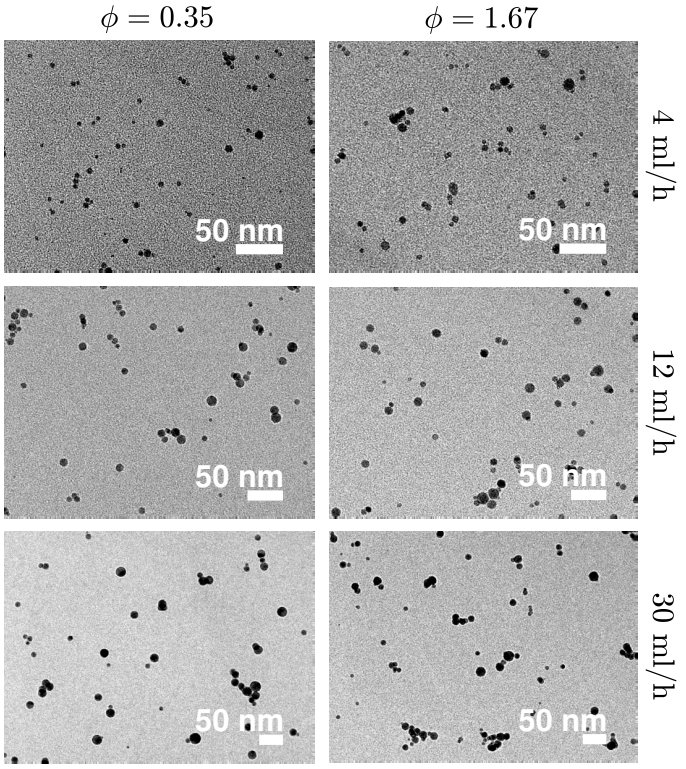

Figure 8: Examples of TEM images used for aggregate size analysis for all conditions tested in this work. In order to minimise bias from particles overlapping, only TEM images with a particle coverage of less than 5% were included in the analysis.

In order to describe the particle morphology, α, the ratio of d_{g} to d_{sph}, is used to characterise the level of particle aggregation. Spherical particles have α close to 0.7 while aggregates with open structure have a larger α. As α is affected by the pixel resolution of the particles, the image magnifications were adjusted for different TTIP loading cases such that the average number of pixels per particle is conserved. This ensures that the particle morphology as characterised by α is comparable across all loadings tested.

Figure 9 shows examples of typical aggregates observed in the aggregate size analysis with their corresponding α. Spherical particles (Fig. 9(a)) are typically characterised by α around 0.7. As the structure becomes more open and non-spherical, α, increases to a maximum of around 1.3.

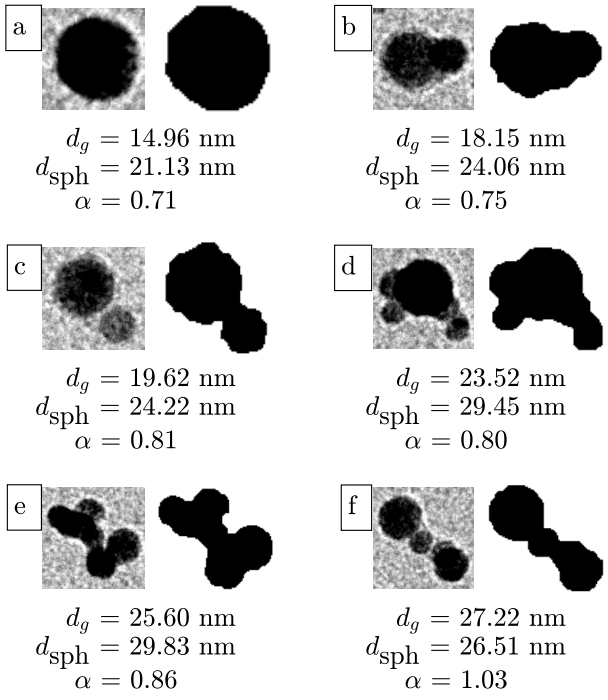

Figure 9: Examples of particles observed in the TEM image analysis and the corresponding pixel mask at varying degree of aggregation (with $\alpha = d_{\text{g}}/d_{\text{sph}}$ ranging from 0.7 to 1). A spherical particle is defined as having $\alpha < 0.73$ in this work.

Figure 10 shows the bivariate histograms of all particles analysed in this work characterised by the parameters d_{sph} and α. Two important observations are made here: First, a significant proportion of particles have α close to 0.7 (shown by the color scale). This is consistent with the qualitative observation that most particles have spherical morphology. Second, larger particles tend to have larger α which is expected as larger particles sinter more slowly leading to the formation of more open structures.

In this work, a condition of $\alpha < 0.73$ is assumed to define a spherical particle. This is slightly higher than a perfect circle whose $\alpha = 0.71$ to allow for some degree of roughness from image analysis algorithm. Table 6 summarises the important metrics of the particle morphology obtained from the aggregate image analysis. Taking into account the size-dependent collection efficiency, $E(d)$ (discussed in Section 4.2.1), an average property, $\bar{X}$, can be calculated as follows

$$\bar{X} = \frac{\sum_i^N X_i / E(d_{\text{sph},i})}{\sum_i^N 1/E(d_{\text{sph},i})}. \tag{29}$$

In all cases, the value of $\bar{\alpha}$, lies within a narrow range of 0.75–0.77 indicating a small degree of particle aggregation which is almost insensitive to the conditions

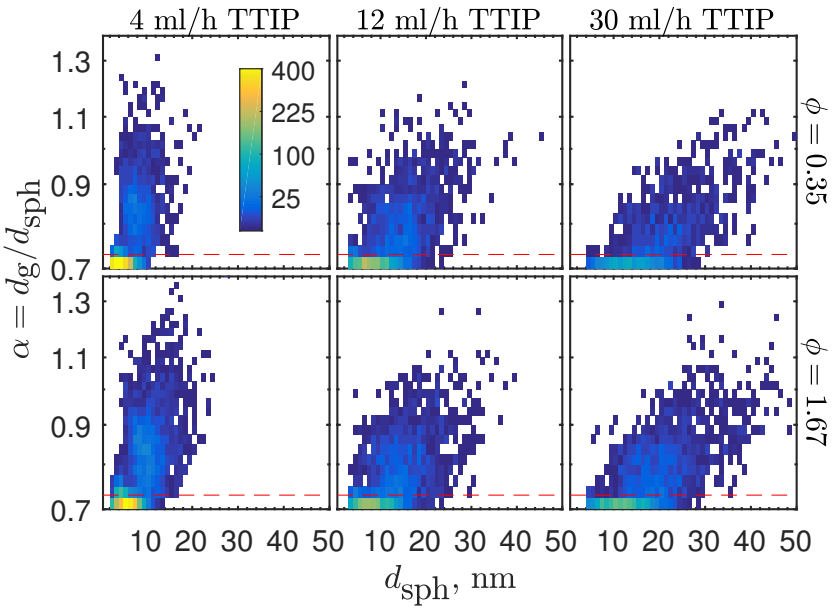

Figure 10: Bivariate histograms of all particles analysed in this work characterised by their geometric parameters d_{sph} and α. The color scale represents particle count. The bin sizes are 1 nm and 0.025 for d_{sph} and α, respectively. The horizontal dashed lines indicate $\alpha = 0.73$.

tested. The degree of aggregation can be further quantified by the proportion of particles with spherical morphology ($\alpha < 0.73$), f, which ranges from 57–68%. This significant proportion of single spherical particles justifies the choice of using d_{sph} as the particle size for TEM collection efficiency and mobility size corrections discussed in Section 4.2.

Table 6: Summary of aggregate size analysis (after size-dependent collection efficiency correction).

ϕ	TTIP (ml/h)	All aggregates				Aggregates, $\alpha < 0.73$		
		count	$\overline{d}_{sph}$ (nm)	$\overline{d}_g$ (nm)	$\overline{\alpha}$	f[a] (%)	$\overline{d}^*_{sph}$ (nm)	Δ[b] (%)
0.35	4	3016	5.81	4.54	0.76	68	4.71	-20.2
0.35	12	2601	10.78	8.37	0.75	64	8.37	-10.0
0.35	30	1582	17.00	13.20	0.75	62	13.27	10.75
1.67	4	3823	7.62	6.10	0.77	57	5.96	-5.2
1.67	12	2676	10.96	8.53	0.76	61	8.45	-0.2
1.67	30	2633	15.49	12.07	0.75	62	11.89	-1.3

[a] $f = [\sum_{\alpha_i<0.73} 1/E(d_{sph,i})]/[\sum_{\text{all } i} 1/E(d_{sph,i})]$
[b] $\Delta = (\bar{d}^*_{sph} - \bar{d}_p)/\bar{d}_p$ (values of $\bar{d}_p$ from Table 5)

Further, the primary size distributions are compared to the aggregate size distributions from the projected area analysis in Fig. 11. The distributions are represented as non-parametric continuous functions (kernel distributions) generated using the kernel density estimator function in MATLAB [7] in order to avoid making any assumptions of the underlying distribution shapes. In general, the aggregate size distributions, d_{sph}, are broader than the primary size distributions, d_p, but the modes of distributions are similar due to the high proportion of single primary particles. The size distributions of particles with $\alpha < 0.73$, denoted as d^*_{sph}, are also shown. It is interesting to note that d^*_{sph} and d_p distributions show relatively good agreement. This suggests that the use of $\alpha < 0.73$ to isolate the spherical particles is appropriate.

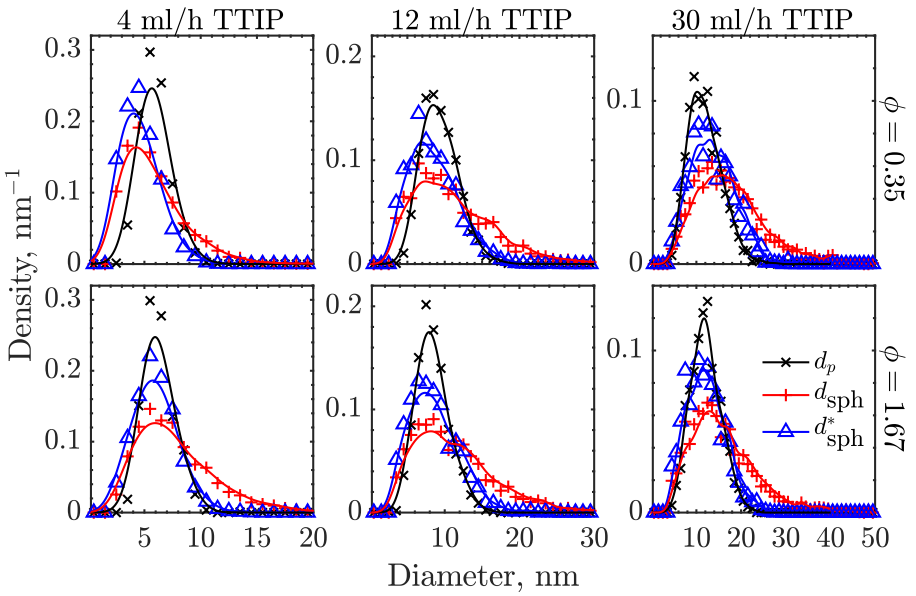

Figure 11: The primary diameter, d_p, and spherical equivalent diameter from aggregate projected area, d_{sph}, distributions for all conditions tested. d^*_{sph} is the spherical equivalent diameter of aggregates with $\alpha < 0.73$ (single primaries). The bin size and the bandwidth for the density estimation are 1 nm.

A rather significant discrepancy is observed for the 4 ml/h case for $\phi = 0.35$ (20%, Table 6). The disagreement between $\bar{d}^*_{\mathrm{sph}}$ from aggregate size analysis and $\bar{d}_p$ from primary particle analysis is likely a result of a bias in the latter towards large particles. This is due to poor contrast and particle overlap especially when the particles are smaller than 4 nm. The comparison of the Sauter mean diameters, $\bar{d}_{3/2}$, for this case shows a smaller difference of 10% suggesting that the discrepancy mainly comes from the left tail of the distribution (small particles).

Lastly, the relatively good agreement between d^*_{sph} and d_p over all conditions, except for the $\phi = 0.35$ flames with low loading cases, tested suggests

that no significant growth through sintering occurs after the aggregation. This likely means that the aggregation does not occur in flame but near the stagnation plate, i.e. if the aggregation happens earlier in flame, further sintering would have resulted in larger primary particles in aggregates compared to non-aggregated spherical particles. This is plausible as the gas temperature only decreases steeply near the stagnation plate [43, 26]. This is supported by the observation that the primary particles in the aggregates are mostly in point contact with small degree of sintering (see Fig. 8).

5. Conclusions

In this work, we demonstrated the use of a TEM sampling method that relies on impaction and diffusion in order to characterise the morphology of titania nano-aggregates prepared in a stagnation flame reactor. TEM images were taken and semi-automated image analysis procedures were performed. The method is validated against electrical mobility measurements taking into account size-dependent collection efficiency of the TEM sampling and mobility size correction. The excellent agreement between TEM-derived and mobility sizes suggests that the TEM sampling combined with image analysis can be used to characterise the particle morphology for the conditions presented here.

The analysis reveals that the primary particle and aggregate sizes are mostly affected by the precursor loading but not the flame temperature. In contrast, the degree of aggregation is found to be insensitive to the precursor loading or the flame temperature. The degree of aggregation is described by α, the ratio of gyration to spherical-equivalent diameters, where spherical particles are defined as having $\alpha < 0.73$. Approximately 60–70% particles analysed have spherical morphology (single spherical particles) while the rest form small aggregated structure with $\alpha = 0.73$–1.3. The aggregation explains the previously observed discrepancy between TEM and mobility sizes. The primary particle size distributions are similar to the spherical particle size distributions which suggests that the aggregation only occurs very late in the particle growth stage (i.e. near the stagnation plate). This is consistent with the qualitative observation of minimal sintering level in the aggregates.

6. Acknowledgements

This project is supported by the National Research Foundation (NRF), Prime Minister's Office, Singapore under its Campus for Research Excellence and Technological Enterprise (CREATE) programme. The authors thank CMCL Innovations for generous financial support. MK also acknowledges the support of the Alexander von Humboldt Foundation.

References

[1] Alderman, O.L.G., Skinner, L.B., Benmore, C.J., Tamalonis, A., Weber, J.K.R., 2014. Structure of molten titanium diox-

ide. Phys. Rev. B - Condens. Matter Mater. Phys. 90, 1–13. https://doi.org/10.1103/PhysRevB.90.094204.

[2] Amin, H.M., Bennett, A., Roberts, W.L., 2018. Determining fractal properties of soot aggregates and primary particle size distribution in counterflow flames up to 10 atm. Proc. Combust. Inst. 37. https://doi.org/10.1016/j.proci.2018.07.057.

[3] Arabi-Katbi, O.I., Pratsinis, S.E., Morrison, P.W., Megaridis, C.M., 2001. Monitoring the flame synthesis of TiO_2 particles by in-situ FTIR spectroscopy and thermophoretic sampling. Combust. Flame 124, 560–572. https://doi.org/10.1016/S0010-2180(00)00227-3.

[4] Balthasar, M., Kraft, M., 2003. A stochastic approach to calculate the particle size distribution function of soot particles in laminar premixed flames. Combust. Flame 133, 289–298. https://doi.org/10.1016/S0010-2180(03)00003-8.

[5] Biskos, G., Reavell, K., Collings, N., 2005. Description and theoretical analysis of a differential mobility spectrometer. Aerosol Sci. Technol. 39, 527–541. https://doi.org/10.1080/027868291004832.

[6] Botero, M.L., Eaves, N., Dreyer, J.A., Sheng, Y., Akroyd, J., Yang, W., Kraft, M., 2018. Experimental and numerical study of the evolution of soot primary particles in a diffusion flame. Proc. Combust. Inst. 37. https://doi.org/10.1016/j.proci.2018.06.185.

[7] Bowman, A.W., Azzalini, A., 1997. Applied smoothing techniques for data analysis: The kernel approach with S-Plus illustrations. OUP Oxford.

[8] Cai, J., Lu, N., Sorensen, C.M., 1993. Comparison of size and morphology of soot aggregates as determined by light scattering and electron microscope analysis. Langmuir 9, 2861–2867. https://doi.org/10.1021/la00035a023.

[9] Camacho, J., Singh, A.V., Wang, W., Shan, R., Yapp, E.K.Y., Chen, D., Kraft, M., Wang, H., 2017. Soot particle size distributions in premixed stretch-stabilized flat ethylene-oxygen-argon flames. Proc. Combust. Inst. 36, 1001–1009. https://doi.org/10.1016/j.proci.2016.06.170.

[10] Chandler, M.F., Yingwu, T., Köylü, Ü.Ö., 2007. Diesel engine particulate emissions: A comparison of mobility and microscopy size measurements. Proc. Combust. Inst. 31 II, 2971–2979. https://doi.org/10.1016/j.proci.2006.07.200.

[11] Frenklach, M., Harris, S.J., 1987. Aerosol dynamics modeling using the method of moments. J. Colloid Interface Sci. 118, 252–261. https://doi.org/10.1016/0021-9797(87)90454-1.

[12] Gonzalez, R.C., Woods, R.E., Eddins, S.L., et al., 2004. Digital image processing using MATLAB.. volume 624. Pearson-Prentice-Hall.

[13] Gopalakrishnan, R., Thajudeen, T., Ouyang, H., Hogan, C.J., 2013. The unipolar diffusion charging of arbitrary shaped aerosol particles. J. Aerosol Sci. 64, 60–80. https://doi.org/10.1016/j.jaerosci.2013.06.002.

[14] Hou, D., Lindberg, C.S., Manuputty, M.Y., Xiaoqing, Y., Kraft, M., 2019. Modelling soot formation in a benchmark ethylene stagnation flame with a new detailed population balance model. Combust. Flame (Accepted for publication) .

[15] Kempema, N.J., Long, M.B., 2016. Combined optical and TEM investigations for a detailed characterization of soot aggregate properties in a laminar coflow diffusion flame. Combust. Flame 164, 373–385. https://doi.org/10.1016/j.combustflame.2015.12.001.

[16] Korobeinichev, O.P., Shmakov, A.G., Maksyutov, R.A., Tereshchenko, A.G., Knyazkov, D.A., Bolshova, T.A., Kosinova, M.L., Sulyaeva, V.S., Wu, J.S., 2012. Synthesis of mesoporous nanocrystalline TiO_2 films in a premixed H_2/O_2/Ar flame. Combust. Explos. Shock Waves 48, 49–56. https://doi.org/10.1134/S0010508212010078.

[17] Kraft, M., 2005. Modelling of particulate processes. KONA Powder Part. J. 23, 18–35. https://doi.org/10.14356/kona.2005007.

[18] Kuga, Y., Okauchi, K., Takeda, D., Ohira, Y., Ando, K., 2001. Classification performance of a low pressure differential mobility analyzer for nanometer-sized particles. J. Nanoparticle Res. 3, 175–183. https://doi.org/10.1023/A:1017952821121.

[19] Lall, A.A., Seipenbusch, M., Rong, W., Friedlander, S.K., 2006. On-line measurement of ultrafine aggregate surface area and volume distributions by electrical mobility analysis: II. Comparison of measurements and theory. J. Aerosol Sci. 37, 272–282. https://doi.org/10.1016/j.jaerosci.2006.01.006.

[20] Li, S., Ren, Y., Biswas, P., Tse, S.D., 2016. Flame aerosol synthesis of nanostructured materials and functional devices: Processing, modeling, and diagnostics. Prog. Energy Combust. Sci. 55, 1–59. https://doi.org/10.1016/j.pecs.2016.04.002.

[21] Li, Z., Wang, H., 2003a. Drag force, diffusion coefficient, and electric mobility of small particles. I. Theory applicable to the free-molecule regime. Phys. Rev. E 68, 1–9. https://doi.org/10.1103/PhysRevE.68.061206.

[22] Li, Z., Wang, H., 2003b. Drag force, diffusion coefficient, and electric mobility of small particles. II. Application. Phys. Rev. E 68, 1–13. https://doi.org/10.1103/PhysRevE.68.061207.

[23] Lindberg, C.S., Manuputty, M.Y., Akroyd, J., Kraft, M., 2019. A two-step simulation methodology for modelling stagnation flame synthesised aggregated nanoparticles. Combust. Flame 202, 143–153. https://doi.org/10.1016/j.combustflame.2019.01.010.

[24] Lindberg, C.S., Manuputty, M.Y., Yapp, E., Akroyd, J., Kraft, M., 2018. A new detailed particle model for polydisperse titanium dioxide aggregates. Submitted for publication .

[25] Manton, M.J., 1979. Brownian diffusion of aerosols to the face of a nuclepore filter. Atmos. Environ. 13, 525–531. https://doi.org/10.1016/0004-6981(79)90146-X.

[26] Manuputty, M.Y., Akroyd, J., Mosbach, S., Kraft, M., 2017. Modelling TiO_2 formation in a stagnation flame using method of moments with interpolative closure. Combust. Flame 178, 135–147. https://doi.org/10.1016/j.combustflame.2017.01.005.

[27] Manuputty, M.Y., Dreyer, J.A.H., Sheng, Y., Bringley, E.J., Botero, M.L., Akroyd, J., Kraft, M., 2019. Polymorphism of nanocrystalline TiO_2 prepared in a stagnation flame: Formation of TiO_2-II phase. Chem. Sci. https://doi.org/10.1039/C8SC02969E.

[28] MATLAB Image Processing Toolbox, 2016b. Matlab image processing toolbox. The MathWorks.

[29] Memarzadeh, S., Tolmachoff, E.D., Phares, D.J., Wang, H., 2011. Properties of nanocrystalline TiO_2 synthesized in premixed flames stabilized on a rotating surface. Proc. Combust. Inst. 33, 1917–1924. https://doi.org/10.1016/j.proci.2010.05.065.

[30] Menz, W.J., Kraft, M., 2013a. A new model for silicon nanoparticle synthesis. Combust. Flame 160, 947–958. https://doi.org/10.1016/j.combustflame.2013.01.014.

[31] Menz, W.J., Kraft, M., 2013b. The suitability of particle models in capturing aggregate structure and polydispersity. Aerosol Sci. Technol. 47, 734–745. https://doi.org/10.1080/02786826.2013.788244.

[32] Ogura, I., Hashimoto, N., Kotake, M., Sakurai, H., Kishimoto, A., Honda, K., 2014. Aerosol particle collection efficiency of holey carbon film-coated TEM grids. Aerosol Sci. Technol. 48, 758–767. https://doi.org/10.1080/02786826.2014.924614.

[33] Ouf, F.X., Yon, J., Ausset, P., Coppalle, A., Maillé, M., 2010. Influence of sampling and storage protocol on fractal morphology of soot studied by transmission electron microscopy. Aerosol Sci. Technol. 44, 1005–1017. https://doi.org/10.1080/02786826.2010.507228.

[34] Pich, J., 1964. Impaction of aerosol particles in the neighbourhood of a circular hole. Collect. Czech. Chem. Commun 29, 2223–2227. https://doi.org/10.1135/cccc19642223.

[35] Ren, Y., Wei, J., Li, S., 2018. In-situ laser diagnostic of nanoparticle formation and transport behavior in flame aerosol deposition. Proc. Combust. Inst. 37. https://doi.org/10.1016/j.proci.2018.06.015.

[36] R'Mili, B., Le Bihan, O.L., Dutouquet, C., Aguerre-Charriol, O., Frejafon, E., 2013. Particle sampling by TEM grid filtration. Aerosol Sci. Technol. 47, 767–775. https://doi.org/10.1080/02786826.2013.789478.

[37] Rudyak, V.Y., Krasnolutskii, S.L., Nasibulin, a.G., Kauppinen, E.I., 2002. Methods of measuring the diffusion coefficient and sizes of nanoparticles in a rarefied gas. Dokl. Phys. 47, 758–761. https://doi.org/10.1134/1.1519325.

[38] Shekar, S., Menz, W.J., Smith, A.J., Kraft, M., Wagner, W., 2012. On a multivariate population balance model to describe the structure and composition of silica nanoparticles. Comput. Chem. Eng. 43, 130–147. https://doi.org/10.1016/j.compchemeng.2012.04.010.

[39] Sheng, Y., Kraft, M., Xu, R., 2018. Emerging applications of nanocatalysts synthesized by flame aerosol processes. Curr. Opin. Chem. Eng. 20, 39–49. https://doi.org/10.1016/j.coche.2018.01.009.

[40] Sorensen, C.M., 2011. The mobility of fractal aggregates: A review. Aerosol Sci. Technol. 45, 765–779. https://doi.org/10.1080/02786826.2011.560909.

[41] Sorensen, C.M., Feke, G.D., 1996. The morphology of macroscopic soot. Aerosol Sci. Technol. 25, 328–337. https://doi.org/10.1080/02786829608965399.

[42] Tammet, H., 1995. Size and mobility of nanometer particles, clusters and ions. J. Aerosol Sci. 26, 459–475. https://doi.org/10.1016/0021-8502(94)00121-E.

[43] Tolmachoff, E.D., Abid, A.D., Phares, D.J., Campbell, C.S., Wang, H., 2009. Synthesis of nano-phase TiO_2 crystalline films over premixed stagnation flames. Proc. Combust. Inst. 32 II, 1839–1845. https://doi.org/10.1016/j.proci.2008.06.052.

[44] Tsantilis, S., Kammler, H.K., Pratsinis, S.E., 2002. Population balance modeling of flame synthesis of titania nanoparticles. Chem. Eng. Sci. 57, 2139–2156. https://doi.org/10.1016/S0009-2509(02)00107-0.

[45] Tsantilis, S., Pratsinis, S.E., 2004. Narrowing the size distribution of aerosol-made titania by surface growth and coagulation. J. Aerosol Sci. 35, 405–420. https://doi.org/10.1016/j.jaerosci.2003.09.006.

[46] Wang, C., Chan, Q.N., Zhang, R., Kook, S., Hawkes, E.R., Yeoh, G.H., Medwell, P.R., 2016. Automated determination of size and morphology information from soot transmission electron microscope (TEM)-generated images. J. Nanoparticle Res. 18, 1–15. https://doi.org/10.1007/s11051-016-3434-x.

[47] Wang, Y., Kangasluoma, J., Attoui, M., Fang, J., Junninen, H., Kulmala, M., Petäjä, T., Biswas, P., 2017. Observation of incipient particle formation during flame synthesis by tandem differential mobility analysis-mass spectrometry (DMA-MS). Proc. Combust. Inst. 36, 745–752. https://doi.org/10.1016/j.proci.2016.07.005.

[48] Warnatz, J., Maas, U., Dibble, R.W., 2006. Combustion: Physical and chemical fundamentals, modelling and simulation, experiments, pollutant formation. 4th ed., Springer.

[49] Xiong, Y., Pratsinis, S.E., 1993. Formation of agglomerate particles by coagulation and sintering – Part I. A two dimensional solution of the population balance equation. J. Aerosol Sci. 24, 283–300. https://doi.org/10.1016/0021-8502(93)90003-R.

[50] Yapp, E.K.Y., Chen, D., Akroyd, J., Mosbach, S., Kraft, M., Camacho, J., Wang, H., 2015. Numerical simulation and parametric sensitivity study of particle size distributions in a burner-stabilised stagnation flame. Combust. Flame 162, 2569–2581. https://doi.org/10.1016/j.combustflame.2015.03.006.

[51] Zhao, B., Uchikawa, K., McCormick, J.R., Ni, C.Y., Chen, J.G., Wang, H., 2005. Ultrafine anatase TiO_2 nanoparticles produced in premixed ethylene stagnation flame at 1 atm. Proc. Combust. Inst. 30, 2569–2576. https://doi.org/10.1016/j.proci.2004.08.146.

[52] Zhao, B., Uchikawa, K., Wang, H., 2007. A comparative study of nanoparticles in premixed flames by scanning mobility particle sizer, small angle neutron scattering, and transmission electron microscopy. Proc. Combust. Inst. 31 I, 851–860. https://doi.org/10.1016/j.proci.2006.08.064.

[53] Zhao, B., Yang, Z., Wang, J., Johnston, M.V., Wang, H., 2003. Analysis of soot nanoparticles in a laminar premixed ethylene flame by scanning mobility particle sizer. Aerosol Sci. Technol. 37, 611–620. https://doi.org/10.1080/02786820300908.